Electronic Supplementary Information

Nickel-mediated dynamic interfaces of dual spillover pathways in $Mo_2C/Ni/Fe_3O_4$ for water splitting

Xu Yue[ab], Lei Zheng[c], Shengli Zhang[c], Yeheng Zhang[ab], Zhiheng Xu[de], Xiaobin Tang[de], Haijun Tao[f], Yuqiao Wang*[ab]

[a] Research Center for Nano Photoelectrochemistry and Devices, School of Chemistry and Chemical Engineering, Southeast University, Nanjing, Jiangsu 211189, China

[b] Yangtze River Delta Carbon Neutrality Strategy Development Institute, Southeast University, Nanjing 210096, China

[c] MIIT Key Laboratory of Advanced Display Materials and Devices, School of Materials Science and Engineering, Nanjing University of Science and Technology, Nanjing 210094, Jiangsu, China

[d] Department of Nuclear Science and Technology, Nanjing University of Aeronautics and Astronautics, Nanjing 211106, China

[e] Key Laboratory of Nuclear Technology Application and Radiation Protection in Astronautics, Ministry of Industry and Information Technology, Nanjing 211106, China

[f] Jiangsu Key Laboratory of Materials and Technology for Energy Conversion, College of Material Science and Technology, Nanjing University of Aeronautics and Astronautics, Nanjing 211100, China

* Corresponding author

E-mail: yqwang@seu.edu.cn (Y. Wang)

1. Computational Methodology

Spin-polarized density functional theory (DFT) calculations were conducted using the Vienna Ab initio Simulation Package (VASP) employing the Perdew-Burke-Ernzerhof (PBE) generalized gradient approximation (GGA) for exchange-correlation interactions. Core-electron interactions were treated through the projector augmented wave (PAW) method with a plane-wave basis set truncated at 400 eV kinetic energy. Structural optimizations proceeded via conjugate gradient minimization until reaching convergence thresholds of 10^{-4} eV for total energy and 0.05 $eV·Å^{-1}$ for residual atomic forces. The heterostructure model incorporated a periodic slab geometry with a 15 Å vacuum spacer along the z-axis to mitigate periodic image interactions. Brillouin zone sampling utilized a Γ-centered 1×1×1 k-point mesh following preliminary tests confirming sufficient convergence. Initial crystallographic configurations for Fe_3O_4, Mo_2C, Ni, and $NiFe_2O_4$ were obtained from the Materials Project Database (materialsproject.org) and subsequently refined through HRTEM-informed structural matching and XRD-pattern validation. The computational model incorporated three primary characteristics: (i) vertically aligned Fe_3O_4 nanocrystals anchored on the thermodynamically stable $Mo_2C(101)$ surface, (ii) Ni_6 clusters strategically positioned at Mo_2C/Fe_3O_4 interfacial regions to replicate experimental observations of Ni nanoparticle segregation, and (iii) a representative 154-atom supercell composition ($Ni_6Fe_{12}O_{16}Mo_{60}C_{60}$) reflecting experimental stoichiometries. Adsorption energetics were subsequently calculated through fundamental thermodynamic analysis using the relation:[1]

$$E_{ads} = E_{adsorbate/substrate} - E_{subtrate} - E_{adsorbate} \#(1)$$

where $E_{adsorbate/substrate}$, $E_{subtrate}$, and $E_{adsorbate}$ represent the total energies of the optimized adsorption system, pristine substrate, and isolated adsorbate molecule, respectively.

The electrochemical reaction free energy (ΔG) was determined by:

$$\Delta G = \Delta E + \Delta ZPE + \Delta TS \#(2)$$

where ΔE denotes the DFT-calculated energy difference between initial and final states, ΔZPE the zero-point energy correction, and ΔTS the entropic contribution at 298.15 K.

Electronic structure analyses included:

Charge transfer density:[2]

$$\rho_{int} = \int \rho_{avg}(z)\, dz \#(3)$$

d-band center position:

$$\varepsilon_d = \frac{\int E \times PDOS_d(E)\, dE}{\int PDOS_d(E)\, dE} \#(4)$$

where $PDOS_d(E)$ represents the projected density of states for *d*-orbitals.

The alkaline oxygen evolution reaction (OER) pathway follows a four-electron mechanism:[3]

$$* + OH^- \rightarrow OH* + e^- \# (5)$$

$$*OH + OH^- \rightarrow O* + H_2O(l) + e^- \# (6)$$

$$*O + OH^- \rightarrow *OOH + e^- \#(7)$$

$$*OOH + OH^- \rightarrow * + H_2O(l) + O_2(g) + e^- \#(8)$$

The hydrogen evolution reaction (HER) proceeds via the Volmer step:[4]

$$* + H_2O(l) + e^- \rightarrow H* + OH^- \#(9)$$

The lattice mismatch was calculated by following equation:

$$\delta = \frac{a_2 - a_1}{a_1} = \frac{\Delta a}{a} \#(10)$$

where a_1 represented the lattice constant of the substrate material and a_2 was the lattice constant of the epitaxial layer material.

2. Preparation of $Mo_2C/Ni/Fe_3O_4$

The homemade Mo_2C nanospheres (0.50 g) were ultrasonically dispersed in 24 mL of ethylene glycol/water mixed solvent (v/v = 1:2) to form a homogeneous suspension. The suspension was magnetically stirred while sequentially adding $FeCl_3 \cdot 6H_2O$ (0.41 g) and $NiCl_2 \cdot 6H_2O$ (0.18 g) until complete dissolution of the metal salts. Subsequently, 32 mL of 4 M NaOH aqueous solution was added dropwise under vigorous stirring, resulting in the formation of a brown colloidal suspension. The mixture was transferred into a 100 mL polytetrafluoroethylene-lined autoclave and hydrothermally treated at 180 °C for 10 h. After natural cooling to room temperature, the product was collected by centrifugation, washed thoroughly with deionized water and ethanol, then vacuum-dried at 60 °C for 12 h to obtain the $Mo_2C/Ni/Fe_3O_4$ composite. For comparison, $NiFe_2O_4$ was synthesized using the identical procedure without the addition of Mo_2C nanospheres. Similarly, pure Fe_3O_4 nanoparticles were prepared by replacing nickel salts with equivalent molar amount of iron salts while omitting the Mo_2C component. Additionally, two physical mixtures ($Mo_2C+NiFe_2O_4$ and

Mo_2C+Fe_3O_4) were prepared by thoroughly grinding the respective components in a 1:1 mass ratio for subsequent comparative studies.

3. Preparation of Mo_2C nanospheres

The Mo-polydopamine precursor was first prepared by dissolving $(NH_4)_6Mo_7O_{24}\cdot 4H_2O$ (0.98 g) and dopamine hydrochloride ($C_8H_{12}ClNO_2$, 0.25 g) in 80 mL deionized water under continuous magnetic stirring for 30 min. To this solution, 160 mL anhydrous ethanol was gradually added, inducing a color transition to bright orange. The pH value was carefully adjusted to 8 using diluted ammonia solution (25 wt%), followed by 6 h aging at room temperature to complete the coordination process. The resulting precipitate was collected via centrifugation, washed alternately with deionized water and ethanol three times, then dried under vacuum at 60 °C for 12 h.Subsequent carbothermal reduction was carried out in a tube furnace under flowing N_2 atmosphere. Approximately 1.0 g of the dried precursor was heated to 800 °C at a controlled ramping rate of 5 °C min^{-1}, maintained at this temperature for 2 h, then allowed to cool naturally to ambient temperature, yielding the final Mo_2C nanospheres.

4. Characterization

The morphological features and elemental composition were investigated using field-emission scanning electron microscopy (FE-SEM, FEI Inspect F50, Thermo Fisher Scientific). High-resolution transmission electron microscopy (HRTEM) and energy dispersive X-ray spectroscopy (EDS) analyses were conducted on a Talos F200X system (Thermo Fisher Scientific). Crystal structure characterization was performed via X-ray diffraction (XRD, Shimadzu XRD-6000) using Cu Kα radiation (λ = 1.5406 Å) over a 2θ range of 10-80°. Surface chemical states were analyzed by X-ray photoelectron spectroscopy (XPS, Thermo Scientific K-Alpha) with charge compensation referenced to adventitious carbon (C 1s at 284.8 eV). Molecular vibration modes were characterized by Raman spectroscopy (Thermo Scientific DXR2) with a 532 nm laser source. Table S7 and S8 summarize key analytical parameters obtained from XPS and EIS measurements, correspondingly.

5. Electrochemical Evaluation

Electrochemical measurements were conducted using a CHI 760E potentiostat (CH Instruments) in a conventional three-electrode configuration in 1 M KOH: Catalyst-modified glassy carbon (GC, 3 mm diameter) as a working electrode, high-purity graphite rod as a counter electrode, and saturated calomel electrode (SCE) as a reference electrode. All potentials were converted to the reversible hydrogen electrode (RHE) scale using:

$$E_{RHE} = E_{SCE} + 0.059 \times pH + 0.241\#(11)$$

Hydrogen evolution reaction (HER) and oxygen evolution reaction (OER) activities were evaluated by linear sweep voltammetry (LSV) at 2 mV s^{-1} with 90% iR compensation. Electrochemical impedance spectroscopy (EIS) measurements spanned 0.01 Hz to 100 kHz with a 10 mV AC amplitude. Double-layer capacitance (C_{dl}) was determined through cyclic voltammetry (CV) in the non-Faradaic region (-0.05-0.05 V vs. SCE) across scan rates of 10-140 mV s^{-1}. Electrochemically active surface area (ECSA) was calculated via:[5]

$$ECSA = \frac{C_{dl}}{C_s}\#(12)$$

where C_s was general specific capacitance of smooth electrode (0.04 mF cm^{-2}).

Hydrogen adsorption/desorption characteristics were probed by CV at elevated scan rates (100-600 mV s^{-1}). Catalytic durability was assessed through chronopotentiometry at 10 mA cm^{-2} for 150 h. Full water splitting tests employed two symmetrical Ni foam electrodes (1 cm^2) loaded with $Mo_2C/Ni/Fe_3O_4$. Gas evolution quantification for Faraday efficiency calculations utilized a calibrated gas chromatograph (GC, Agilent 7890B).

The Mott-Schottky is performed by coating the catalyst on ITO glass in 0.5 M Na_2SO_4. The flat band potential (E_{fb}) is obtained by Mott-Schottky equation:

$$\frac{1}{C^2} = \frac{2}{e\varepsilon\varepsilon_0 N_d}\left[\left(E - E_{fb}\right) - \frac{\kappa T}{e}\right]\#(13)$$

where E_{fb} is the flat band potential.

The carrier density was calculated by fitting slope of Mott-Schottky curve:

$$N_D = \frac{2}{\varepsilon_r \varepsilon e k}\#(14)$$

where N_D was carrier density, k was fitting slope.

6. Catalyst ink preparation

2.0 mg catalyst powder was homogenized with 0.5 mg acetylene black and 50 μL Nafion solution (5 wt%) in 2.0 mL ethanol/water (v/v=1:1) via 30-minute ultrasonication. A precisely controlled 20 μL aliquot was drop-casted onto the GC substrate, achieving a mass loading of 0.42 mg cm^{-2} after vacuum drying at 60°C.

Supplementary Figures

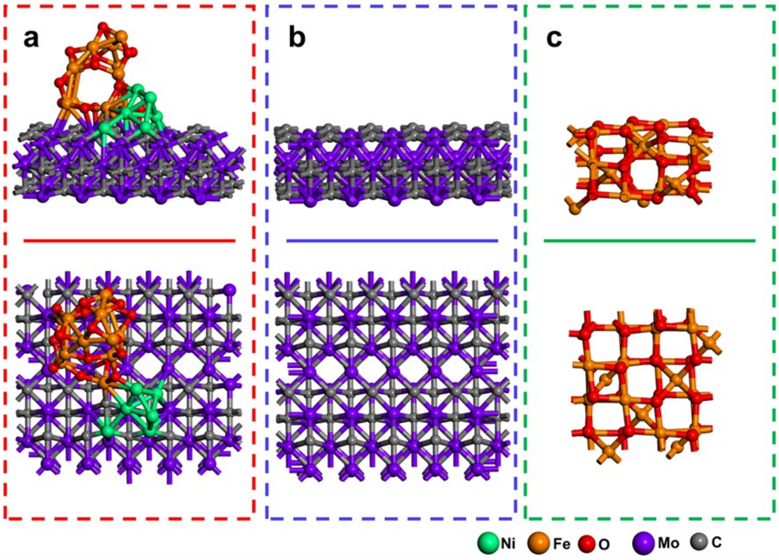

Fig. S1 Theoretical calculation model (a) $Mo_2C/Ni/Fe_3O_4$ (b) Mo_2C (c) Fe_3O_4.

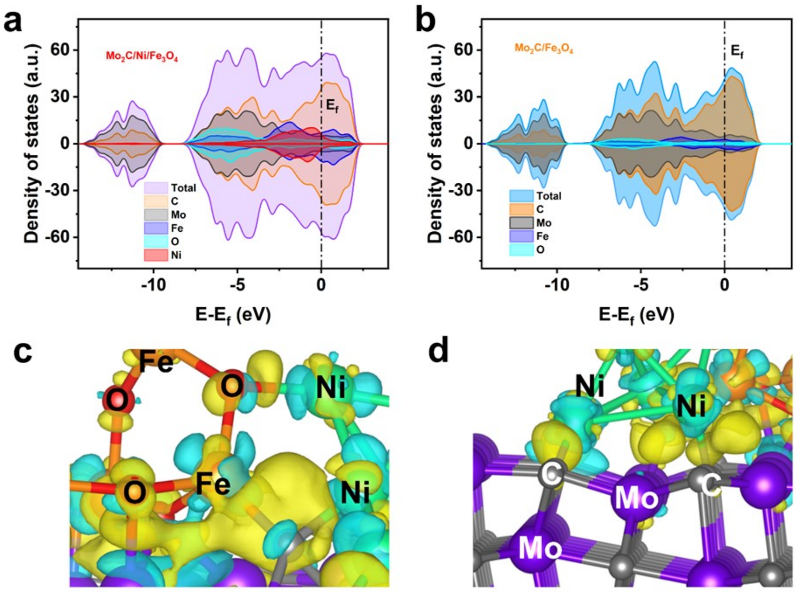

Fig. S2 Electron density of states for (a) $Mo_2C/Ni/Fe_3O_4$ and (b) Mo_2C/Fe_3O_4. Charge density differences with and without the Ni interlayer at (c) Ni/Fe_3O_4 interface and (d) Mo_2C/Ni interface.

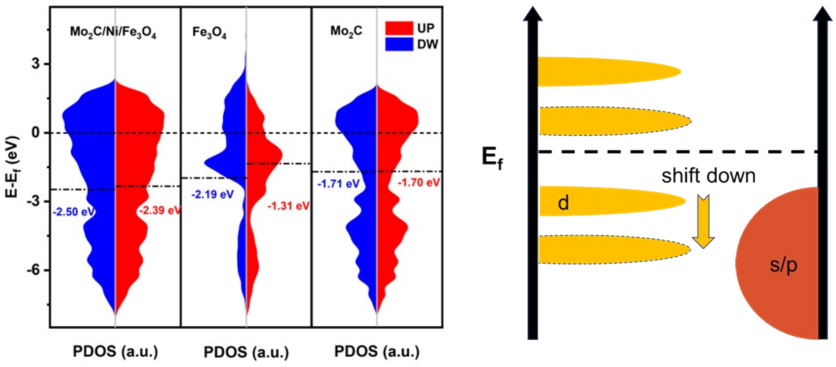

Fig. S3 Projected density of states of *d*-orbit and diagram of downshifted d-band interaction with *s*, *p* orbital.

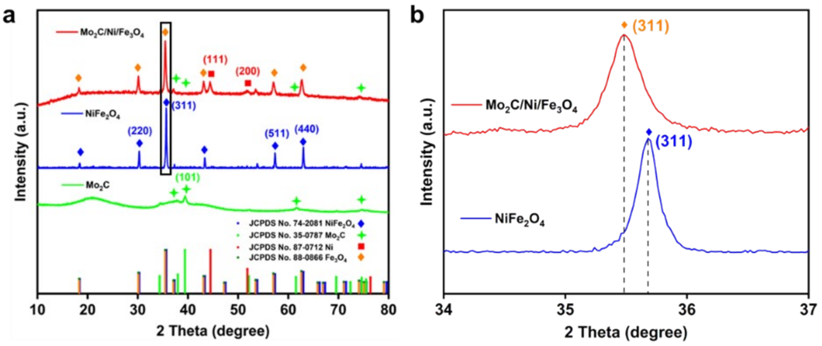

Fig. S4 (a) XRD spectra of the as-fabricated Mo_2C, $NiFe_2O_4$, and $Mo_2C/Ni/Fe_3O_4$. (b) The local amplification diagram of (311) peak.

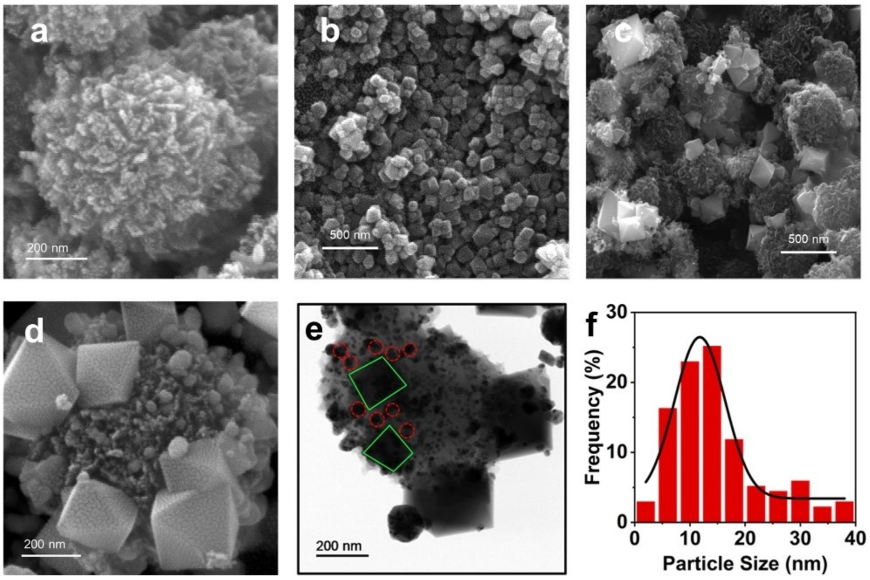

Fig. S5 SEM images of (a) Mo_2C, (b) $NiFe_2O_4$ and (c) $Mo_2C+Fe_3O_4$ and (d) $Mo_2C/Ni/Fe_3O_4$. (e) TEM images of $Mo_2C/Ni/Fe_3O_4$. (f) Particle size statistics of surface Ni particles.

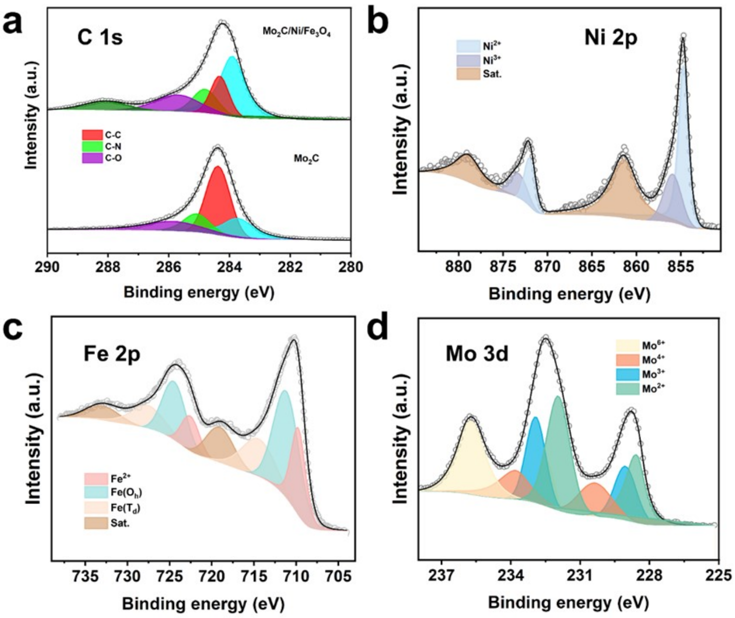

Fig. S6 High-resolution XPS spectra: (a) C 1s in $Mo_2C/Ni/Fe_3O_4$ and Mo_2C, (b) Ni 2p and (c) Fe 2p for $NiFe_2O_4$, (d) Mo 3d for Mo_2C.

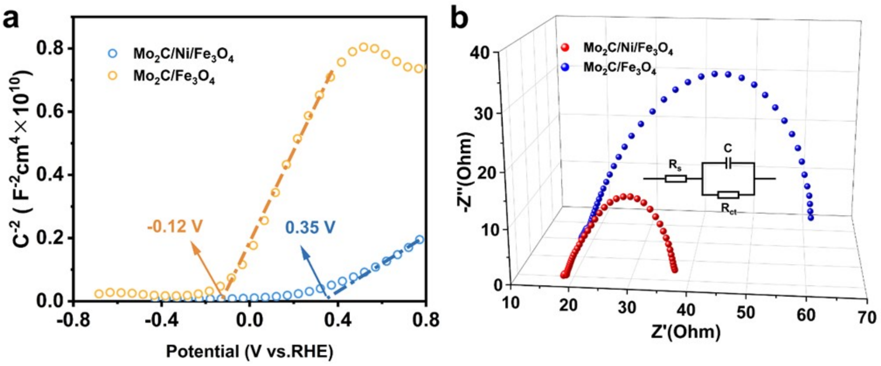

Fig. S7 (a) Mott-Schottky curves and (b) Nyquist plots for $Mo_2C/Ni/Fe_3O_4$ and Mo_2C/Fe_3O_4.

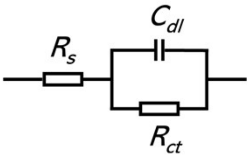

Fig. S8 The equivalent circuit model fitted by the electrochemical impedance spectroscopy data.

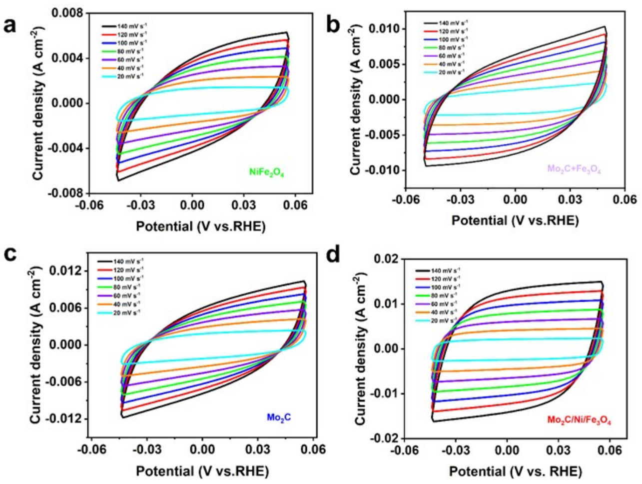

Fig. S9 Cyclic voltammetry curves of (a) $NiFe_2O_4$, (b) Mo_2C/ Fe_3O_4, (c)Mo_2C and (d) $Mo_2C/Ni/Fe_3O_4$.

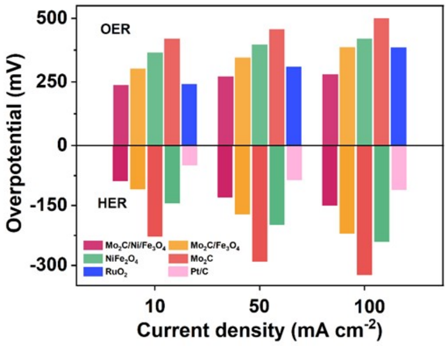

Fig. S10 The overpotential values of the $Mo_2C/Ni/Fe_3O_4$, Mo_2C/Fe_3O_4, $NiFe_2O_4$, Mo_2C, Pt/C, and RuO_2 at 10, 50, and 100 mA cm^{-2}.

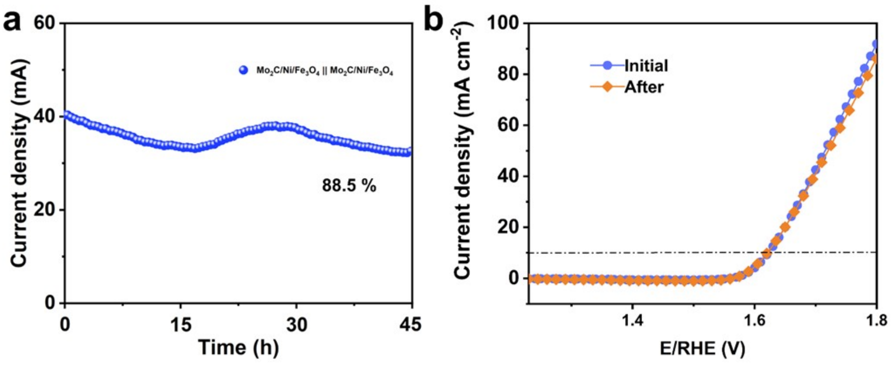

Fig. S11 (a) Current density-time curves of fully water splitting devices. (b) LSV curves of the fully water splitting devices before and after stability test.

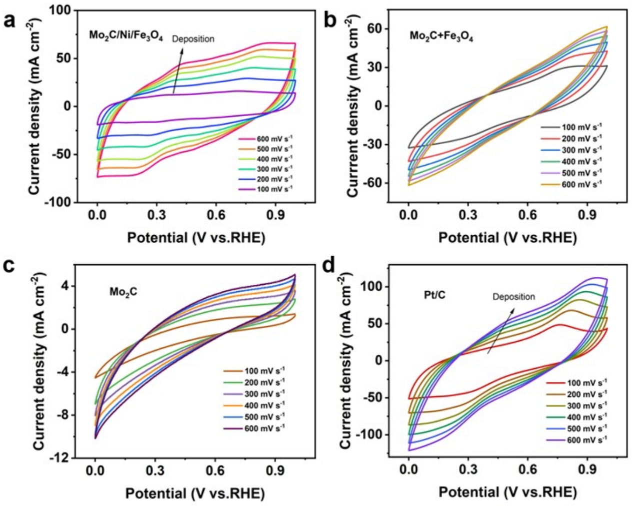

Fig. S12 Cyclic voltammetry curves of (a) $Mo_2C/Ni/Fe_3O_4$, (b) $Mo_2C+Fe_3O_4$, (c) Mo_2C and (d) Pt/C.

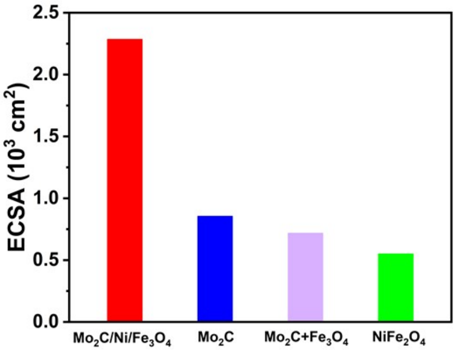

Fig. S13 Comparative analysis of electrochemical active surface area.

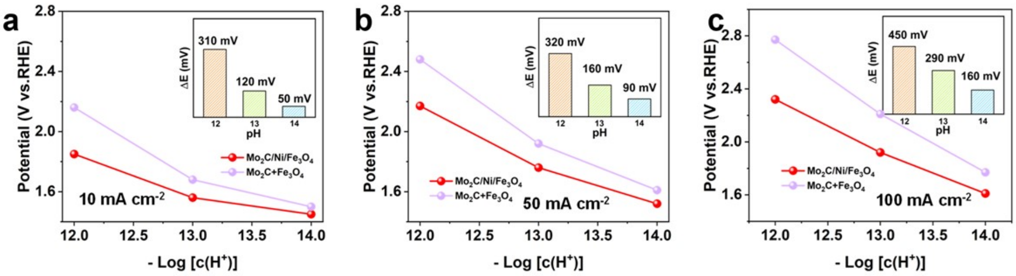

Fig. S14 Potential plots *vs.* pH at different current densities: (a) 10, (b) 50 and (c) 100 mA cm^{-2}.

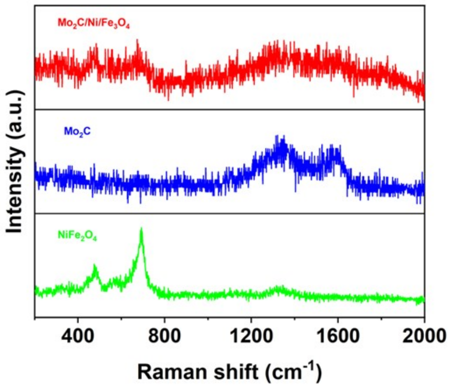

Fig. S15 Raman spectra of the as-synthesized Mo_2C, $NiFe_2O_4$, and $Mo_2C/Ni/Fe_3O_4$.

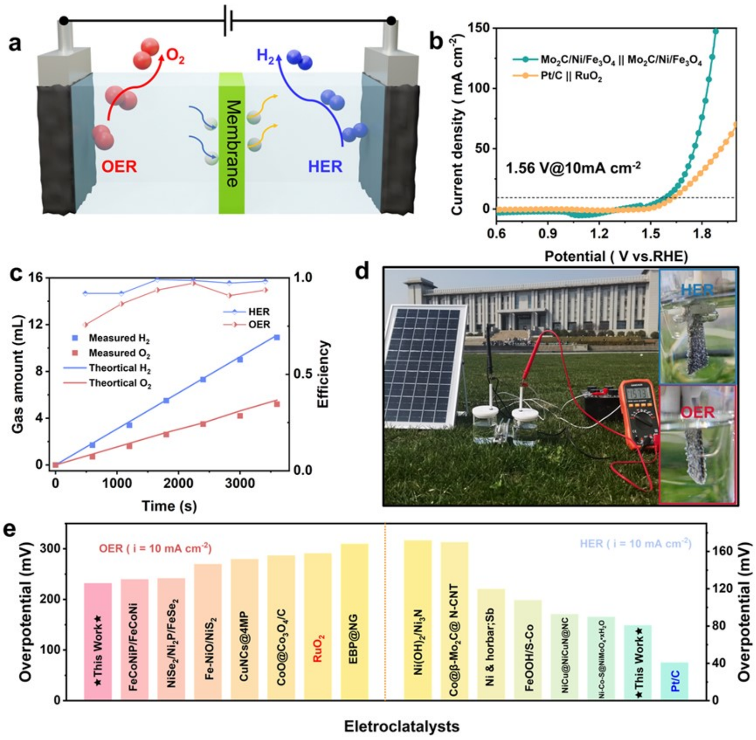

Fig. S16 (a) Diagram of anion-exchange membrane water electrolytic cell. (b) The performance comparison of $Mo_2C/Ni/Fe_3O_4$ with commercial electrolytic Pt/C and RuO_2. (c) Faradaic efficiency. (d) Solar-driven electrolytic cell. (e) Comparison with the reported multi-component catalysts (Table S7, S8).

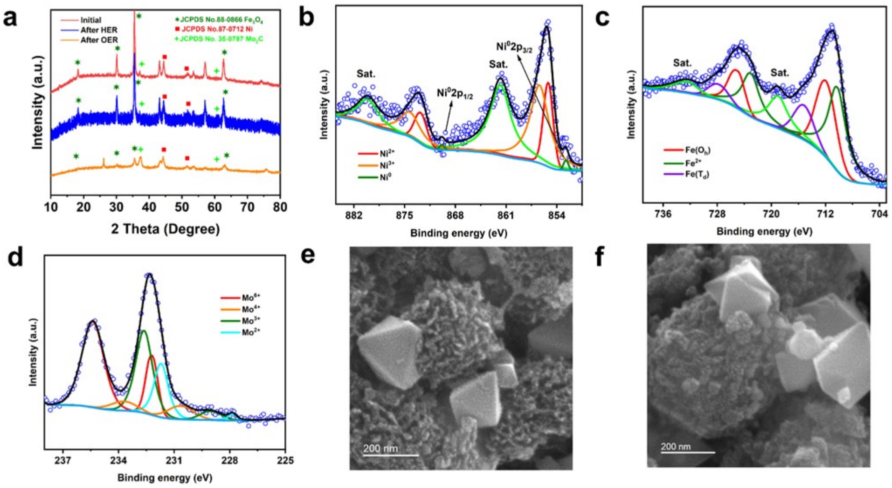

Fig. S17 (a) XRD pattern of the $Mo_2C/Ni/Fe_3O_4$ after HER and OER. High-resolution of (b) Ni 2p, (c) Fe 2p and (d) Mo 3d spectra of $Mo_2C/Ni/Fe_3O_4$ after OER for 10 h. SEM images of microstructure after (e) HER and (f) OER for 10 h.

Supplementary Tables

Table S1. Parameters for lattice strain calculations.

Crystal cell	**a×b×c**
Ni	3.5238×3.5238×3.5238
Fe_3O_4	8.3847×8.3847×8.3847
Mo_2C	3.0124×3.0124×4.7352

Table S2. Key parameters derived from Nyquist plot fitting during HER.

Parameter	**$Mo_2C/Ni/Fe_3O_4$**	**Mo_2C**	**$Mo_2C+Fe_3O_4$**
R_s (Ω cm²)	2.1 ± 0.1	2.3 ± 0.2	2.4 ± 0.3
R_{ct} (Ω cm²)	9.9 ± 0.4	18.4 ± 0.7	23.8 ± 1.1
C_{dl} (mF cm⁻²)	12.7 ± 0.5	8.2 ± 0.3	6.9 ± 0.4
C_{dl} (mF cm⁻²)*	90.1	34.3	28.7
Tafel Slope (mV dec⁻¹)	57.7 ± 1.2	195.8 ± 3.1	126.3 ± 2.5
Dominant Mechanism	Heyrovsky-controlled	Volmer-limited	Volmer-Heyrovsky

* Experimental data calculated by CV plots.

Table S3 Key parameters derived from Nyquist plot fitting during OER.

Parameter	**$Mo_2C/Ni/Fe_3O_4$**	**$NiFe_2O_4$**	**$Mo_2C+NiFe_2O_4$**
R_s (Ω cm²)	1.1 ± 0.1	1.0 ± 0.3	1.3 ± 0.2
R_{ct} (Ω cm²)	39.5 ± 1.1	127.6 ± 4.1	68.3 ± 2.3
C_{dl} (mF cm⁻²)	90.1 ± 3.2	22.9 ± 1.4	54.7 ± 2.1
C_{dl} (mF cm⁻²)*	90.1	22.7	28.7
TOF (s⁻¹)	0.45	0.09	0.28

* Experimental data calculated by CV plots.

Table S4 Key parameters derived from EIS plot fitting (η=200 mV):

Parameter	**$Mo_2C/Ni/Fe_3O_4$**	**$Mo_2C+Fe_3O_4$**
R_2 (Ω cm^2)	12.7	38.4
C_φ (mF cm^{-2})	4.51	1.60
τ ($R_2 \times C_\varphi$, ms)	57.3	61.4

Table S5. Tafel slope of $Mo_2C/Ni/Fe_3O_4$ at different pH conditions.

pH	**η_{10} (mV)**	**Tafel Slope (mV dec^{-1})**
14	228	42.3
13	348	61.7
12	658	89.4

Table S6. XPS result of $Mo_2C/Ni/Fe_3O_4$, $NiFe_2O_4$ and Mo_2C

Elements	$Mo_2C/Ni/Fe_3O_4$	$NiFe_2O_4$	Mo_2C	Assignment
	Component(eV)/ Content (at, %)	Component(eV)/ Content (at, %)	Component(eV)/ Content (at, %)	
C 1s	283.9/41.5%	–	283.7/20.3%	C-M
	284.3/16.7%		284.4/45.5%	C-C
	284.8/14.0%		285.1/14.7%	C-N
	285.9/18.1%		286.1/19.5%	C-O
	288.1/9.7%		–	O=C-O
Mo 3d	228.6/4.5%		228.5/13.0%	+2 ($3d_{5/2}$)
	229.6/4.5%		229.2/10.0%	+3 ($3d_{5/2}$)
	231.2/5.0%		230.5/9.9%	+4 ($3d_{5/2}$)
	232.2/22.3%		232.0/22.2%	+2 ($3d_{3/2}$)
	232.7/38.4%		232.5/5.4%	+6 ($3d_{5/2}$)
	233.3/18.0%		232.9/13.7%	+3 ($3d_{3/2}$)
	234.2/2.7%		233.9/8.7%	+4 ($3d_{3/2}$)
	235.9/47.1%		235.7/18.1%	+6 ($3d_{3/2}$)
Fe 2p	710.6/16.9%	709.8/14.3%	–	+2 ($2p_{3/2}$)
	712.0/26.9%	711.3/27.2%		+3 (O_h)
	715.7/16.8%	714.8/13.9%		+3 (T_d)
	720.1/5.4%	719.3/10.0%		Sat.
	723.3/9.4%	722.6/6.5%		+2 ($2p_{1/2}$)
	725.6/11.6%	724.8/13.6%		+3 (O_h)
	729.6/10.1%	727.8/9.3%		+3 (T_d)
	734.2/2.9%	733.3/5.2%		Sat.
Ni 2p	852.6/12.4%	–		+0 ($2p_{3/2}$)
	855.1/27.3%	854.7/31.8%		+2 ($2p_{3/2}$)
	856.4/15.0%	856.0/13.1%		+3 ($2p_{3/2}$)
	861.7/17.6%	861.4/28.9%		Sat.
	871.7/5.7%	–		+0 ($2p_{1/2}$)
	872.5/3.7%	872.2/7.6%		+2 ($2p_{1/2}$)
	873.8/6.7%	873.4/6.7%		+3 ($2p_{1/2}$)
	879.5/11.6%	879.3/11.9%		Sat.

Table S7. A summary of the OER performance based on various catalysts in 1 M KOH.

Catalysts	Overpotential (10 mA cm^{-2})	Reference
$Mo_2C/Ni/Fe_3O_4$	**228 mV**	**This work**
RuO_2	**291 mV**	**This work**
$Fe\text{-}NiO/NiS_2$	270 mV	[6]
FeCoNiP/FeCoNi	240 mV	[7]
CuNCs@4MP	280 mV	[8]
$CoO@Co_3O_4/C$	287 mV	[9]
$NiSe_2/Ni_2P/FeSe_2$	242 mV	[10]
EBP@NG	310 mV	[11]

Table S8. A summary of the HER performance based on various catalysts in 1 M KOH.

Catalysts	Overpotential (10 mA cm^{-2})	Reference
Pt/C	**55 mV**	**This work**
$Mo_2C/Ni/Fe_3O_4$	**80 mV**	**This work**
EBP@NG	170 mV	[11]
FeOOH/S-Co	108 mV	[12]
$Ni\text{-}Co\text{-}S@NiMoO_4·xH_2O$	90 mV	[13]
NiCu@NiCuN@NC	93 mV	[14]
$Ni(OH)_2/Ni_3N$	172 mV	[15]
Ni & horbar;Sb	119 mV	[16]

Reference

1. X. Zhang, S. Zhu, L. Song, Y. Xu and Y. Wang, *Nanoscale*, 2023, **15**, 3764-3771.
2. T. Lu and Q. Chen, *ChemPhysChem*, 2021, **22**, 386-395.
3. B. Zhang, X. Shang, Z. Jiang, C. Song, T. Maiyalagan and Z. Jiang, *ACS Appl. Energy Mater.*, 2021, **4**, 5059-5069.
4. P. Kuang, T. Tong, K. Fan and J. Yu, *ACS Catal.*, 2017, **7**, 6179-6187.
5. C. Wei, S. Sun, D. Mandler, X. Wang, S. Z. Qiao and Z. J. Xu, *Chem. Soc. Rev.*, 2019, **48**, 2518-2534.
6. N. Zhang, Y. Hu, L. An, Q. Li, J. Yin, J. Li, R. Yang, M. Lu, S. Zhang, P. Xi and C. H. Yan, *Angew. Chem., Int. Ed.*, 2022, **61**, e202207217.
7. G. Wang, H. Zou, H. Zhang, J. Xiang, M. Yang and J. Liu, *Electrochim. Acta*, 2023, **462**, 142723.
8. V. Saini, Krishankant, S. Choudhary, A. Gaur, S. Banerjee, V. Bagchi and V. Venkatesh, *J. Mater. Chem. A*, 2023, **11**, 24754-24763.
9. H. Chu, D. Zhang, P. Feng, Y. Gu, P. Chen, K. Pan, H. Xie and M. Yang, *Nanoscale*, 2021, **13**, 19518-19526.
10. J. Yin, C. Wang, J. Li, K. Zhang, Z. Wu, N. Wang and Y. Du, *Nanoscale*, 2023, **15**, 4523-4528.
11. Z. Yuan, J. Li, M. Yang, Z. Fang, J. Jian, D. Yu, X. Chen, L. Dai, *J. Am. Chem. Soc.*, 2019, **141**, 4972-4979.
12. Z. Zang, Y. Ren, X. Li, Y. Cheng, L. Li, X. Yu, X. Yang, Z. Lu, X. Zhang and H. Liu, *J. Mater. Chem. A*, 2023, **11**, 24618-24628.
13. Z. Gao, T. Zhang, D. Xu, P. Liu, H. Liu, H. Li, Y. Liu, F. Yu and G. Wang, *J. Catal.*, 2024, **434**, 115540.
14. J. Hou, Y. Sun, Z. Li, B. Zhang, S. Cao, Y. Wu, Z. Gao and L. Sun, *Adv. Funct. Mater.*, 2018, **28**.
15. C. E. Chukwuneke, K. Kawashima, H. Li, R. A. Marquez, Y. J. Son, L. A. Smith, H. Celio, G. Henkelman and C. B. Mullins, *J. Mater. Chem. A*, 2024, **12**, 1654-1661.
16. V. K. Mariappan, K. Krishnamoorthy, P. Pazhamalai, R. Swaminathan, S.-J. Kim, *Small*, 2024, **20**, 2402355.